Measurement 175 (2021) 109049

Contents lists available at ScienceDirect

Measurement

journal homepage: www.elsevier.com/locate/measurement

Multi-sensor imagery rectification and registration for herbicide testing

Francisco Agüera-Vega [a,*], Marta Agüera-Puntas [a], Juan Agüera-Vega [b], Patricio Martínez-Carricondo [a], Fernando Carvajal-Ramírez [a]

[a] Departamento de Ingeniería, Universidad de Almería, Almería, Spain, Campus de Excelencia Internacional Agroalimentaria ceiA3, Centro de Investigación Mediterráneo de Economía y Desarrollo Sostenible, Spain
[b] Departamento de Ingeniería Rural, Universidad de Córdoba, Córdoba, Spain, Campus de Excelencia Internacional Agroalimentaria ceiA3

ARTICLE INFO

Keywords:
Image registration
Multispectral images
Thermal images

ABSTRACT

The use of multi-spectral sensors has been focused on several agricultural tasks, yet it is necessary to further assess this approach to achieve sufficient precision to carry out adequately these. Metric information from these images is traditionally derived by photogrammetric techniques, but with a major limitation: photographed objects should be static while the photographs are being taken, but plants are generally in movement because of wind and this causes the photogrammetric process to be unable to generate the necessary information to make any metric measurement. To bypass this, metric information can be derived via rectification, using only one photograph.

This work aims to develop a band co-registration method with agricultural purposes, based on rectified images taken from different sensors usually mounted on UAVs or terrestrial vehicles, studying its accuracy in a quantitative way. All multispectral information co-registered in a precise way will allow the calculation or development of new radiometric and even geometric indices that will help to improve efficiency in many tasks related to agriculture.

Images taken from a multi-spectral (green, near infra-red, red and red edge) and a thermal camera were used to apply the developed methodology. First, a digital elevation model describing the displacement produced by distortion due to the sensor lens was obtained and applied to each of the studied pictures to correct this distortion. Then, distortion due to conic perspective present in the photographs was corrected, taking into account the homology relationship between the photographed object and the picture. To carry out these tasks, several computers programs were developed. Subsequently, the edges of the five bands corresponding to 250 plants were digitalised and their areas were measured. Furthermore, the intersection of the five bands of each plant was calculated, and an index (*AI*) indicating the fraction of the area of each band, which was out of the common area edge of the five bands, was calculated for each plant. The average value of this index for each band ranged from 0.22 to 0.24, with no statistically significant differences between them, indicating a high accuracy of the proposed methodology.

1. Introduction

Discrimination of plants of different species, identification of some of their morphological characteristics, and knowledge of their physiological status is crucial in many tasks related to agriculture. One of these tasks is the precision weeding, which uses located spraying and physical weed control. This is environmentally friendly, safe for health, and has economic benefits [1]. For precision weeding is essential the discrimination of weeds from crops. Most of the studies related to this discrimination have focused on the spectral information-based methods [2–6].

Furthermore, there are rules for the authorisation of herbicides in commercial form and their placing on the market [7]. A dossier including data related to effectiveness, occurrence or possible occurrence of resistance development, adverse effects on treated crops on other undesirable or unintented side-effects is required. Therefore, trials should be designed to investigate all those specified issues, to minimise the effects of random variation between different parts of each site and

* Corresponding author at: Departamento de Ingeniería. Universidad de Almería, Almería, Spain, Campus de Excelencia Internacional Agroalimentaria ceiA3, Spain.
E-mail address: faguera@ual.es (F. Agüera-Vega).

https://doi.org/10.1016/j.measurement.2021.109049
Received 27 September 2019; Received in revised form 16 December 2020; Accepted 14 January 2021
Available online 7 February 2021

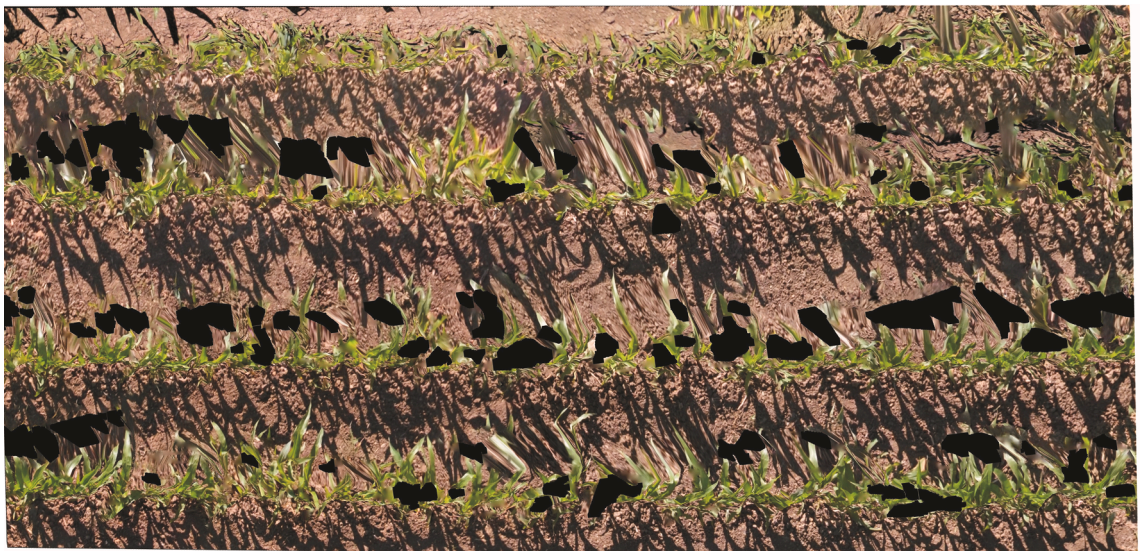

Fig. 1. Orthophoto of a maize plot obtained from photographs taken at low wind conditions. The black spots represent the areas where the orthophoto could not be generated. There are other areas where the image is blurred or not congruent. Orthophoto from previous studies of the authors.

to enable statistical analyses to be applied to results amenable to such analyses. The data derived from these trials must referred to each of the species under study and therefore, the species must be discriminated previously. Qualitative methods, also called visual evaluation methods, have been widely used to evaluate herbicide performance due their practicality, although they show a number of limitations [8]. To bypass these limitations, development of objective and affordable methodologies could be based, as precision weeding, on spectral and morphological information.

Knowledge of the crop water, nutritional or health status is essential if sustainable crop management and efficient use of inputs are to be achieved. Again, many studies related to these objectives are based on spectral information [9–13].

Another important task in the field of agriculture is the collection of data in crop breeding programs. Phenotyping provides important support for crops breeding because it profiles crop geometric traits (e.g., leaf area index (LAI), plant height), physiological traits (e.g. contents of chlorophyll and other pigments), indicator of abiotic and biotic stress (e.g. leaf water potential, canopy temperature differences), nutrient contents (e.g. nitrogen content) and yield [14–17]. Since the counting of these traits must often be done under field conditions and hundreds of test plots are required, field breeding measurements are time-consuming and expensive. To avoid these problems, phenotyping based on radiometric information is constantly developing since from this type of data, methodologies can be developed to quickly quantify the traits under study [10,18–20].

Spectral indices, which are combinations of spectral measurements at different wavelengths, are used to derive the required information in all those mentioned agricultural tasks [6]. Therefore, multispectral or even hyperspectral sensors are mounted on different types of platforms (satellites, aircraft, terrestrial vehicles, or unnamed aerial vehicles (UAVs)) to carry out radiometric measurements. When high spatial and/or temporal resolution is required, appropriate platforms are terrestrial vehicles and UAVs because they can operate as close to the object as required and because they are less dependent on weather conditions [15,21]. On these platforms, it is common to mount multi-sensor devices (for example MiniMCA-12, http://www.tetracam.com/, Micasense Redege, https://micasense.com/ or Parrot Sequoia, https://parrot.com/), even several devices mounted on the same platform (multispectral sensor and thermal infrared sensor, for example).

On the other hand, spectral sensor data are pictures represented in conic perspective, without any metric properties. If the scene under study is photographed from different points of view, orthorectification techniques yield a scaled orthogonal projection of this scene, called orthophoto, enabling subsequent measurements.

One of the limitations of orthorectification is that photographed objects must be static while the photographs are being taken. If the objects are waggling, the result will be an incomplete orthophoto or, in extreme cases, it will not be possible to obtain the orthophoto [22]. This circumstance can occur in agricultural scenes with low wind speeds. Fig. 1 represents an orthophoto of a maize crop plot obtained from photographs taken by the authors at low wind conditions (3–7 km $\times$ h^{-1}). Consequently, there are areas where the orthophoto could not be generated (black spots) and other areas where the image is blurred or is not congruent.

To bypass this limitation, another photogrammetric technique can be used: rectification. As rectification uses only one photograph, the movement of the photographed objects will not be a problem. There are two image rectification methods: polynomial rectification and projective rectification [23]. Both polynomial and projective methods have a common limitation: they do not adequately correct relief displacement and therefore, they only work properly if the photographed objects are contained in a plane. Nevertheless, these methods, especially the projective method, are typically used to rectify aerial photographs of flat terrain or images of building facades, with only slight undulations. If agricultural studies are carried out in flat plots and when the crop is not very high, photographic rectification using the projective method could be an alternative to orthorectification to generate information, thereby avoiding the problem of the photographed objects in movement.

Furthermore, multi-spectral or multi-sensor images show significant band misregistration effects due to lens distortion and the different point of view of each lens or sensor [24–27]. Consequently, to obtain accurate spectral and geometrical information, a precise geometric distortion correction and band-to-band registration method is necessary.

In general, the image registration process presents four steps [28]: feature extraction, feature matching, image transformation and image interpolation. The feature extraction and matching steps find the same points in all bands and construct the connection among them, determined by an image transformation model. The image interpolation step preserves the image radiometric information after the transformation model is applied. Proposed methodologies for image registration vary in the feature detection methods and in the adopted image transformation model [24–27,29]. Anyway, in the scientific literature, there is a lack of studies related to single-image registration and to the quantitative

Fig. 2. Multi-spectral Sequoia camera (left) and sunshine sensor (right).

accuracy of the results because, in general, it is very difficult task.

In this context, this work aims to develop a band co-registration method with agricultural purposes, based on rectified images taken from different sensors usually mounted on UAVs or terrestrial vehicles, studying its accuracy in a quantitative way. All multispectral information co-registered in a precise way will allow the calculation or development of new radiometric and even geometric indices that will help to improve efficiency in many tasks related to agriculture.

2. Material and methods

2.1. Imaging system

The imaging system was composed of a four-band Parrot Sequoia multispectral camera and a Workswell WIRIS 2nd gen thermal camera. The Sequoia camera has received increased attention from remote sensing users because of its small size and for being one of the lightest imaging systems on the current market. Furthermore, its adopted narrow band is better suited for detecting the plants' spectral reflectance. It has five lenses, four of them have a sensor resolution of 1280 × 960 pixels, 1.2 megapixels, a size of 4.8 × 3.6 mm, and collect data in discrete spectral bands: Green (GRE, 550 nm, 40 nm bandwidth), Red (RED, 660 nm, 40 nm bandwidth), Red Edge (REG, 735 nm, 10 nm bandwidth) and Near Infrared (NIR, 790–40 nm bandwidth), with a 10-bit depth. The fifth lens can acquire a higher resolution (4608 × 3456, 16 megapixels) broadband RGB image. Another sunshine sensor should be mounted together with the camera for accurate radiometric correction. The monochrome cams have a focal length of 4.0 mm, with a horizontal field of view (FOV) of 61.9° and a vertical FOV of 48.5°. Fig. 2 shows this camera and the sunshine sensor.

The Workswell WIRIS 2nd gen thermal camera (Fig. 3) used in this study has a resolution of 640 × 512 pixels, with a temperature sensitivity of up to 0.03 °C and a temperature range from −25 to 150 °C; it contains a lens of 19 mm, which represents a horizontal FOV of 32° and a vertical FOV of 26°. The sensor has a size of 10.88 × 8.705 mm and collects data in the range from 75 to 135 nm. This system has an RGB camera with a resolution of 1600 × 1200 pixels, 1.9 megapixels.

Due to their dimensions and weights, both cameras are appropriate for being mounted on a UAV or on a terrestrial vehicle.

2.2. Field experiment

The field experiment was carried out in a sunflower (*Helianthus annuus*, L.) crop located in Córdoba, Spain (349042, 4,198,307 UTM coordinates, zone 30), when the plants had about four to eight leaves and a height of approximately 8 to 20 cm. Furthermore, some weed species were present (*Chenopodium album,* L., *Convolvulus arviensis,* L.; and *Cyperus rotundus,* L.), all of them in early development stage. A graduate rectangular frame of 57 × 47 cm was used as reference to scale and identify equivalent points in all bands. The frame was posed on the ground surrounding some sunflower and weed plants (Fig. 4). Subsequently, a picture was taken with the multispectral and thermal cameras, which were mounted on a platform, including the power supply, voltage regulators, a radio control to shoot the thermal camera and a monitor. This platform was transported by an operator who framed the scene, while another operator was in charge of shooting both cameras, the thermal one with the radio control station and the multispectral one through the mobile phone's WiFi. A total of 100 shoots were made with

Fig. 4. The frame used in the experiment.

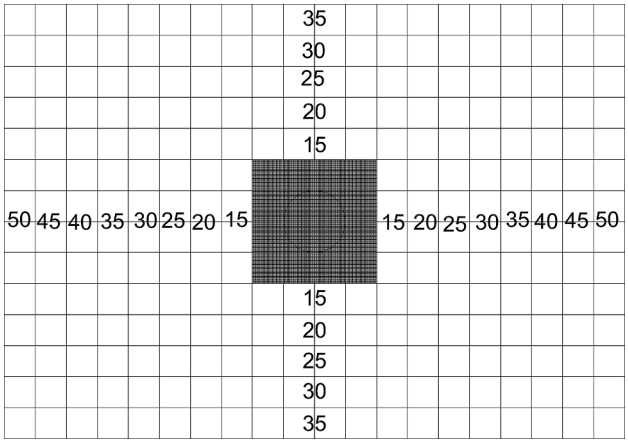

Fig. 5. Grid used for correcting distortions by lens.

Fig. 3. Workswell WIRIS 2nd gen thermal camera.

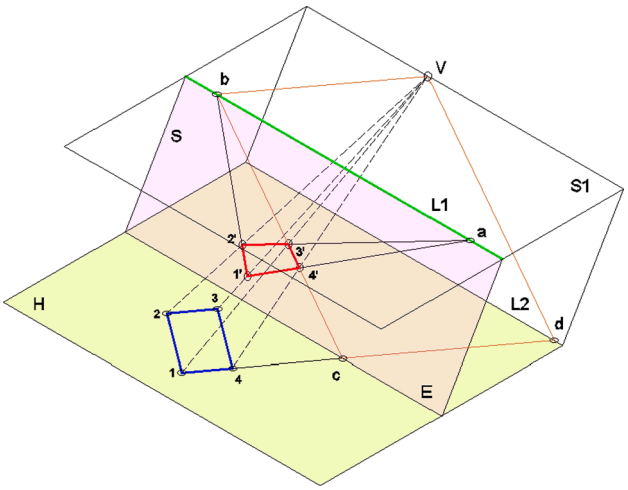

Fig. 6. Elements of the homology relationship between the image and the photographed object.

each sensor, and thus, resulting in a total of 500 images, 100 × 4 from each shoot of multispectral camera and 100 × 1 from the thermal camera. The distance from the cameras to the plants was approximately between 2 and 3 m, which is equivalent to distances used when terrestrial vehicles or UAVs at low flight altitude are used as platforms [30].

2.3. Band-to-band co-registration

Band co-registration was carried out in two steps. The first one eliminated the lens distortions, and the second one corrected the perspective distortion. A detailed explanation of each step is given in the following sections.

2.3.1. Lens distortion correction

To correct lens distortion, a grid of 50 × 50 mm was printed on a 1000 × 700 mm paper format which was fixed to a vertical plane, with the grid lines being oriented vertically and horizontally (Fig. 5).

Subsequently, for each of the used cameras, a picture of the grid was obtained with the optical axis perpendicular to the grid plane. In this way, sensor and grid planes were parallel, and the grid and the image had an affine relationship.

Furthermore, the images were affected by lens distortion, and distorted images were loaded on a computer-aided design program (AutoCAD 2019) and scaled. The coordinates of each grid vertex in the distorted image (x_{Di}, y_{Di}), were recorded and compared with the real coordinates in the printed grid (x_{Ri}, y_{Ri}) to calculate the error in the X ($\varepsilon_X = x_{Ri}\text{-}x_{Di}$) and in the Y ($\varepsilon_Y = y_{Ri}\text{-}y_{Di}$) components. Since each band has a different location when the picture is taken, all the vertices of the grid do not appear in each band Then, the number of vertices studied (i) varied from 89 to 95, depending on the image (band) considered. Based on these data, digital elevation models (DEMs) of ε_X and ε_Y components were computed, with a resolution coinciding with the image resolution (1280 rows by 960 columns for GRE, NIR, RED and REG bands and 640 rows by 512 columns for the thermal band (THE)), using the inverse distance to a square power interpolation method. These DEMs of distortion errors indicate the displacements in X and Y directions to be applied to each pixel to correct the lens distortions and are applicable to all images taken with these cameras. A computer program was developed to correct the images, taking into account the error grids. Previously, to correct lens distortion, another computer program was developed to mark and save the coordinates of the four frame vertexes. This program shows the image and the frame vertexes should be manually marked.

2.3.2. Conic perspective distortion correction

All images taken with a lens system represent a central projection (conic perspective) of the photographed objects. Considering that these objects are flat and that all of them are included in the same plane, effects of the central projection, produced because the object and sensor planes are not parallel, will be as follows: a) straight parallel lines in the scene will appear convergent in the image, and b) for objects with the same size, those closer to the camera appear in the image larger than those further away. In addition, it is necessary to take into account the deformation caused in the image by the lack of perpendicularity between the optical axis of the camera and the photographed plane. The geometric relationship between the object and its image is called homology, as mentioned in the introduction section. Fig. 6 represents a detailed graphical homology relationship. In this figure, points 1, 2, 3 and 4 represent a rectangle contented in the plane H, while 1′, 2′, 3′ and 4′ represent the central projection (photography) of the rectangle on the plane S (cam sensor). The point V is the vertex of the homology (focus of the lens), and the intersection between S and H is E, the axis of the homology.

Consequently, from the coordinates in the picture of points 1′, 2′, 3′ and 4′ and knowing the dimensions of the rectangle 1, 2, 3, 4, the homology can be defined and applied to all the pixels of the picture to obtain a representation without distortions.

A computer program was developed to rectify the images. The inputs of this program were the dimensions (length and width) of the frame described in Section 2.2 and the pixel coordinates of the frame vertices, measured on the lens distortion-corrected images. From these data, the homology between the image and the reality was established based on its geometric properties: all homologue straight lines have the cut point contained in the axis E of the homology (point c in the Fig. 6), and two homologous points are connected by a straight line containing the vertex of the homology. Then, this geometric relation was applied to all image pixels. At the end of this process, some pixels in the corrected image have no digital value because the established homology does not shift any pixels to that position. To solve this problem, the digital value of these pixels is estimated by interpolation. Image interpolation was carried out using the value of the nearest pixel, but any interpolation method could be implemented. When the image is rectified, it is clipped to only include the area in the reference frame. Thus, images are co-registered taking as reference the frame vertices.

2.4. Assessment of images correction and band co-registration accuracy

After correction of lens and perspective distortions, images of the same plant in each band may be different in size and shape due to errors inherent in the correction processes: aiming error when pointing at the vertices of the frame, error in the correction of lens distortions, and error in the correction of perspective. In addition, the co-registration process also involves the commission of an error that accumulates to the previous ones. To assess the accuracy of the whole process described in this work, after lens and perspective distortion corrections and co-registration, 250 individual plants, including crop and weed plants, were selected from the 100 shoots made with each sensor. The contour of each of these plants was manually digitalised using AutoCAD 19. As a result, 1250 contours, five for each plant corresponding to GRE, RED, NIR, REG and THE band, were used. Furthermore, the area of each digitalised contour was calculated and the intersection (common area) of the five contours corresponding to each plant was determined.

The assessment of the accuracy was quantified taking into account an index based on the areas (*AI*), as follows:

$$AI = \frac{A_{bj} - A_j}{A_{bj}} \quad (1)$$

where:

A_{bj}: area corresponding to the band b (b = GRE, RED, NIR, REG and

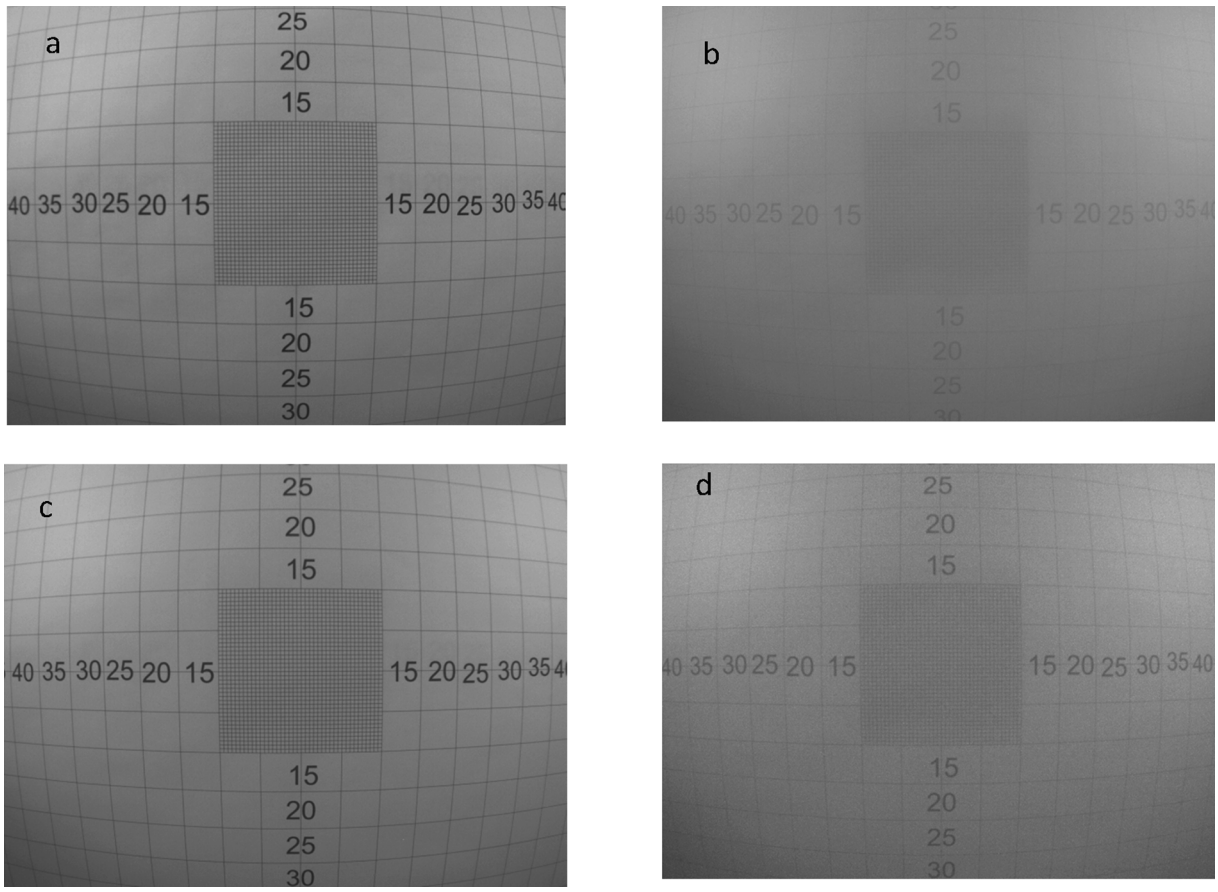

Fig. 7. Images of the grid described in Section 2.3.1 (Fig. 6), taken by a multi-spectral camera at a distance of 60 cm: GRE (a), NIR (b), RED (c) and REG (d).

THE) of the plant *j*;

A_j: area corresponding to the intersection of contours of the five bands of the plant *j*.

This index ranges from 0 to 1 and indicates, for each band, the fraction of the area which is out of the common area of the five bands. For a given band of a given plant, a null value of *AI* indicates that the corresponding contour matches exactly with the contour corresponding to the common area of the five bands. The ideal situation would be that, for each plant, the contours corresponding to each of the bands would have a zero value of *AI*, which indicates that the correction and co-registration process error was null. On the other hand, *AI* greater than zero indicates that the corresponding contour does not exactly match the contour of the common area. The extreme case will be when $AI = 1$, which will indicate that the contours corresponding to the plant under study have no common area.

Subsequently, a statistical analysis of this index was carried out to quantify the accuracy of the described methodology. Statistics (mean value, standard deviation, standard kurtosis and standard skewness) were calculated for each band taking into account the 250 digitized contours on each. In addition, to test for significant differences amongst the *AI* values of each band, an ANOVA was carried out.

3. Results and discussion

3.1. Grid image lens distortion correction

Fig. 7 shows the images of the grid described in Section 2.3.1 (Fig. 5), taken by the multi-spectral camera at a distance of 60 cm. The four images show similar barrel distortion, which becomes more noticeable at the edge of the image. This was expected, since the four lenses and sensors have the same geometry.

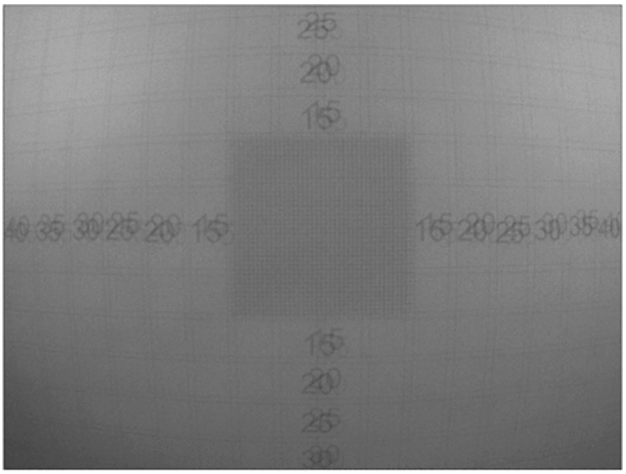

Fig. 8. Overlapping of the four Sequoia bands where the misregistration effects can be observed.

Misregistration effects between each band can be observed in Fig. 8, created from the overlapping of the four multispectral camera bands.

This illustrates that if no band co-registration is conducted, it is not possible to obtain accurate spectral information for multi-spectral image analysis, as described previously [25,27,31]. As explained in Section 2.3.1, ε_X and ε_Y were calculated, and error DEMs were computed. Fig. 9 shows the contour line representation of the ε_X DEMs (left column), ε_Y DEMs (central column), even the composed XY error (right column), for each band of the SEQ camera. Distortion values are expressed in mm. As can be observed, the shapes of contour lines shown in each column as

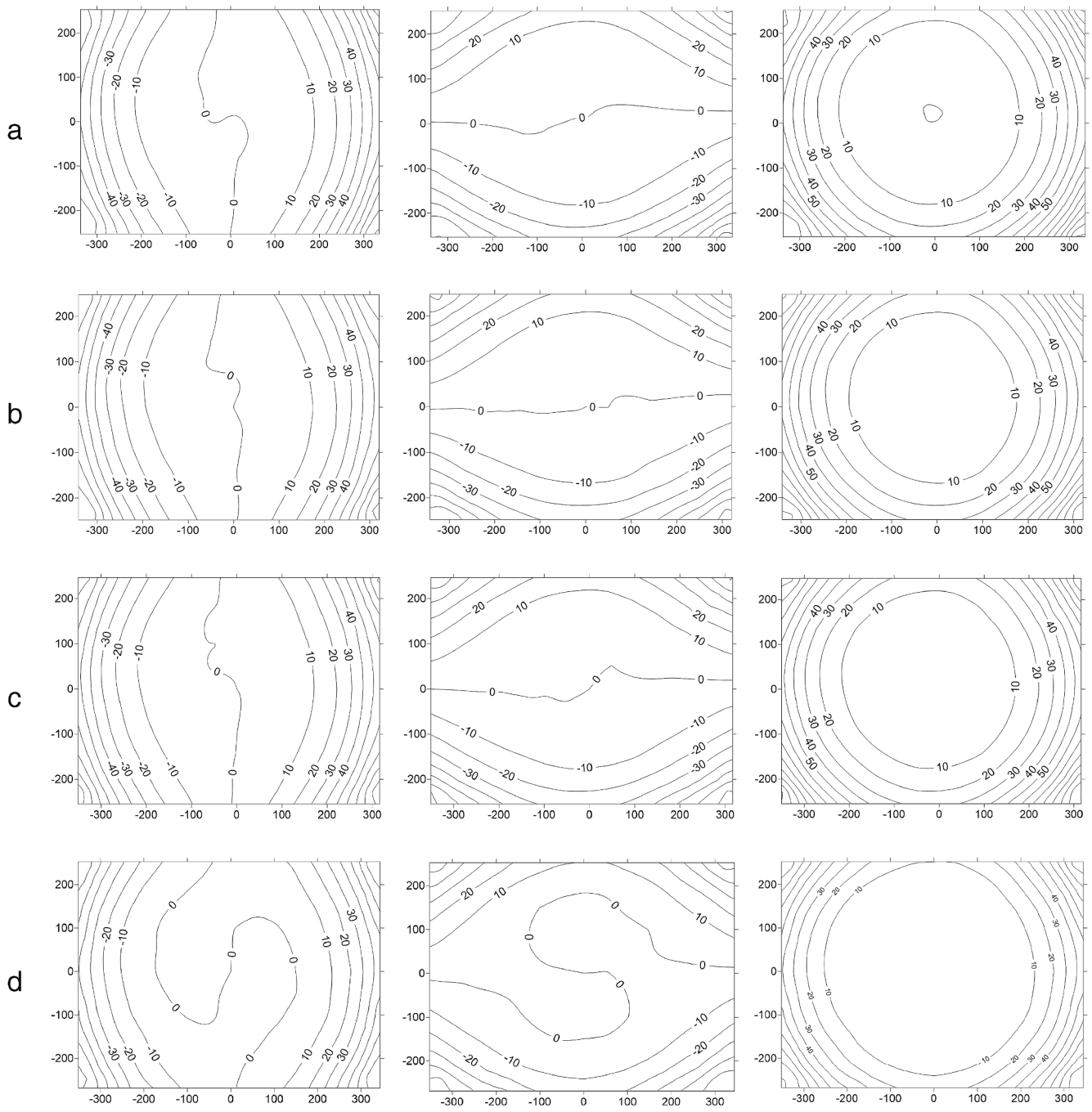

Fig. 9. Contour line representation of the pixel displacement DEMs caused by lens distortion for each Sequoia band: GRE (row a), NIR (row b), Red (row c) and REG (row d). Left column corresponds to ε_X, the centre column corresponds to ε_Y, and the right column represents the composed ε_{XY}. Values are expressed in mm.

similar to what was expected, because the lens and sensors have the same geometry. Furthermore, distortions showed a typical radial pattern, increasing from the centre of the image, where distortion is near zero, to the edge, where distortion reaches its maximum value. In the case of thermal camera, values of ε_X and ε_Y were practically zero and therefore radial distortion was negligible.

3.2. Rectification of field images

In this section, the developed computer program and the partial results of each step of the field image rectification process will be exposed.

3.2.1. Control points

The control points, used for correcting the distortion due to the perspective (central projection), were the four corners of the frame previously described. They were marked on each of the studied images, using the computer program described in Section 2.3.1. The outputs of this program were two files, one for the five bands of multispectral camera and other for the thermal camera, containing the coordinates of the corners of each studied image.

3.2.2. Lens distortion correction

The rectification process consisted of a first step to correct the distortions caused by the lens, applying the displacement DEMs generated for each band. The inputs for the computer program developed for this

Fig. 10. Image 39, NIR band of multi-spectral cam before (left column) and after (right column) lens distortion.

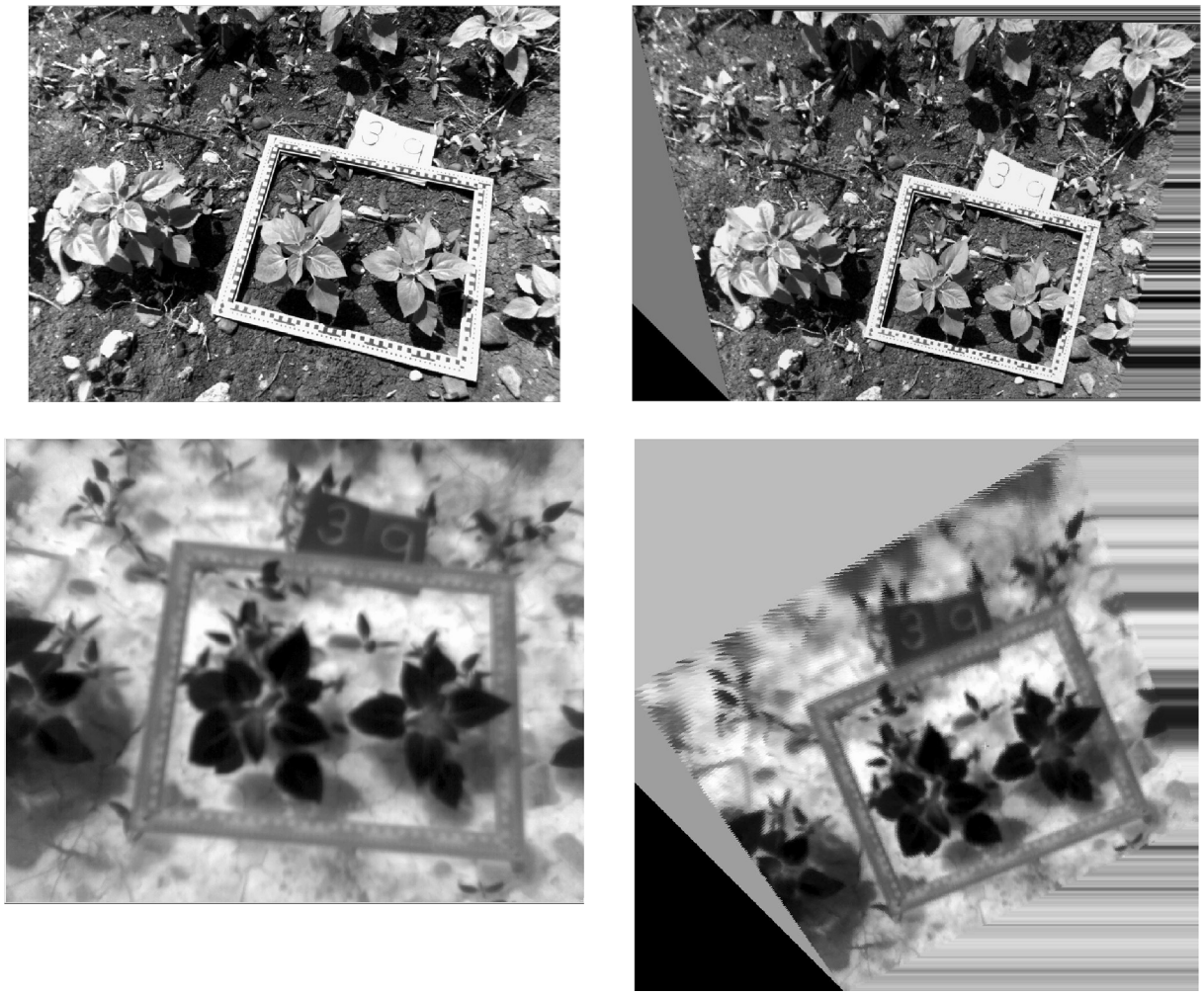

Fig. 11. First partial result of the perspective image correction for sample 39. In the top, the GRE band and in the bottom, the THE band. In the left column, the distorted images, and in the right column, the corrected images.

task were the image to be corrected and the displacement DEM corresponding to this image. The outputs were the corrected image and the transformed coordinates of the four control points. Fig. 10 shows an example of an image (image 39, band NIR) before (left) and after (right) distortion correction. Distortion of monochromatic bands of the multispectral camera were more evident that those in the thermal image.

3.2.3. *Perspective correction*

The inputs of the computer program developed to correct the perspective distortion were the image and the coordinates of the four control points (corners of the frame) after lens distortion correction, and the outputs were the rectified image and the corrected coordinates of the cornerś frame. First, the computer program calculates the homology

Fig. 12. Rectified bands of sample 9: GRE (a), NIR (b), RED (c), REG (d), THE (e).

parameters to transform the distorted frame in a rectangle and then applies this transformation to the entire image. An example of the result of this transformation is shown in Fig. 11, where the GRE (top) and THE (bottom) band images corresponding to sample 39 are shown before (left column) and after (right column) the perspective correction.

To correct the distortion, the process transforms the initial rectangle shape of the image in a trapeze, as shown in the right column of Fig. 10.

3.2.4. *Image co-registration*

The last step of the process is image co-registration. The computer program developed for this task sets the GRE band as reference, extracts the area that covers the frame of the image and rotates it to leave the larger sides of the rectangle in horizontal position. Through an affine transformation, the program makes the co-registration of the rest of the bands by fitting every frame vertex to its equivalent in the GRE band. Fig. 12 shows the results for sample 9.

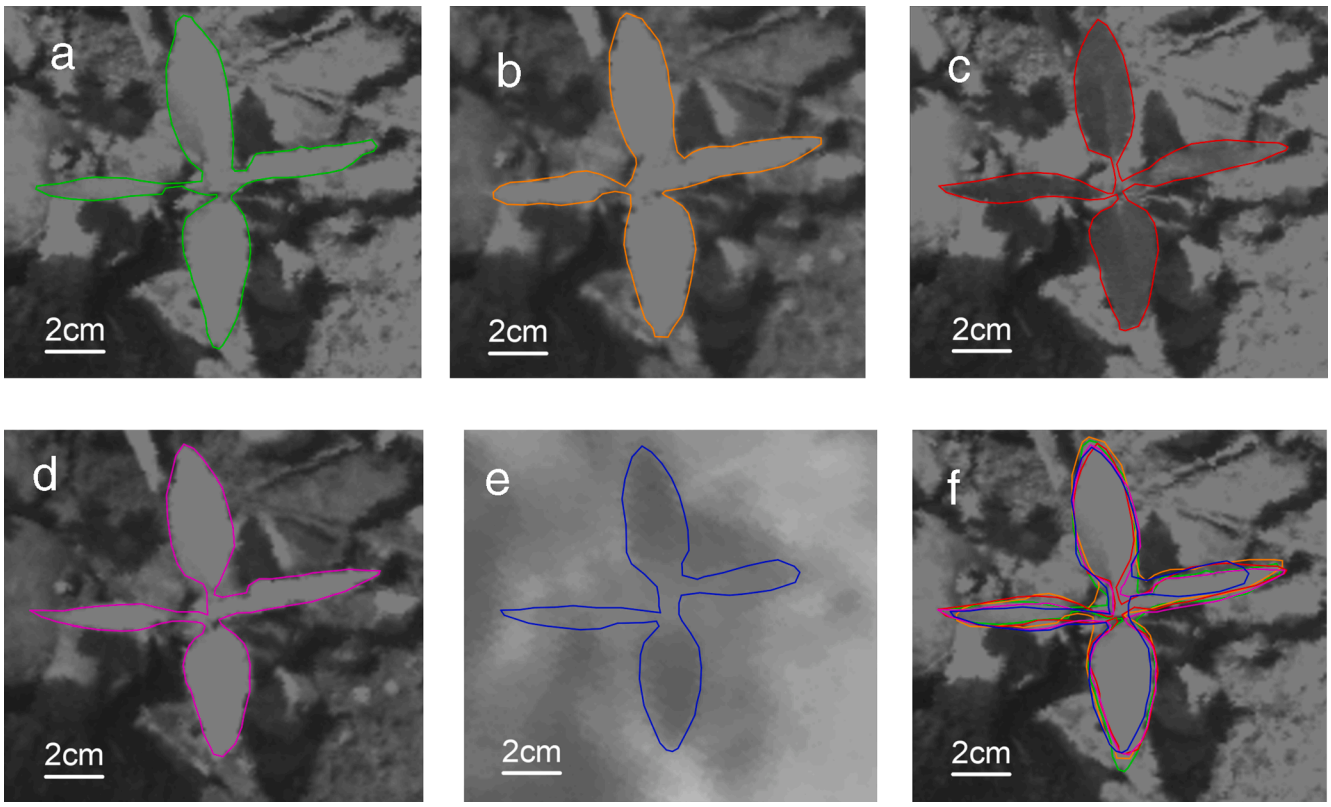

Fig. 13. Example of edge plant digitalisation; a: GRE, b: NIR, c: RED, d: REG, e: THE band, and f: the five edges superposed on the GRE band. (For interpretation of the references to colour in this figure legend, the reader is referred to the web version of this article.)

Table 1
Summary statistics derived from the *AI* indices (Eq. (1)) calculated for each band of each studied plant.

Band	Count	Minimum	Maximum	Range	Average	Standard deviation	Stnd. skewness	Stnd. kurtosis
GRE	250	0.011	0.460	0.449	0.217	0.10120	0.4784	−0.8162
NIR	250	0.012	0.430	0.418	0.241	0.11320	−0.0508	−1.2904
RED	250	0.010	0.434	0.424	0.222	0.11927	0.1230	−1.5176
REG	250	0.013	0.433	0.420	0.220	0.12001	−0.3400	−1.7546
THE	250	0.014	0.485	0.471	0.237	0.12905	1.1579	0.3287
Total	1250	0.010	0.485	0.475	0.226	0.11078	0.6779	1.1746

3.3. Image correction and band co-registration accuracy

Fig. 13 shows an example of plant edge digitalisation for each band (a: GRE, b: NIR, c: RED, d: REG, e: THE band, and f: the five edges superposed on GRE band). Ground sample distance of the images was around 1 mm per pixel. In this graphical representation, the good matching between bands can be appreciated, which was confirmed by subsequent statistical analysis.

Table 1 shows the summary statistics derived from the *AI* indices (Equation (1)), indicating the fraction of area of each band which is out of the five bands (common area) calculated for each band of each studied plant. All maximum and minimum values, and the ranges, were similar. Minimum *AI* values ranged from 0.010 for the GRE band to 0.014 for the THE band, while maximum values ranged from 0.430 for the NIR band to 0.485 for the THE band. Range values were similar for all studied bands, ranging from 0.418 for NIR band, to 0.471 for THE band. The average values showed a narrow range of variation between bands: from 0.217 for GRE band to 0.237 for THE band. The results of future classifications to differentiate between crops and weeds will be more accurate as the *AI* value for the plant under study is closer to zero. In any case, the mean value of *AI* obtained in this study is close enough to zero to state that the location of the plant, as well as the area it occupies, will be calculated with sufficient precision to be of assistance in different agricultural tasks, such as weed control using precision farming techniques, or the study of the evolution of the amount of weeds in an experimental field crop.

Furthermore, standard skewness and standard kurtosis values within the range −2 to + 2, as shown for all *AI* data in Table 1, are expected for data from a normal distribution. Fig. 14 shows the *AI* frequency histograms for each band, all of them presenting a typical shape of a normal distribution. ANOVA for multiple test comparison was carried out, and no statistically significant differences between means at the 95% confidence level were found.

As already mentioned in the introduction section, so far, only few studies were related to single image registration and quantitative accuracy of the results and most of them measure it in pixel units. For example, [24] proposed a two-fold solution for seamless band-to-band registration of images captured by five different sensors integrated into a miniature multi-spectral camera system. They concluded that their method is adaptable to both close-range and aerial applications with an accuracy higher than 0.3 pixels. This work even shows an example of applying this technique in the images taken from an agricultural field and, although the error of co-registration is not quantified, it is qualitatively acceptable, which agree with our quantitative results.

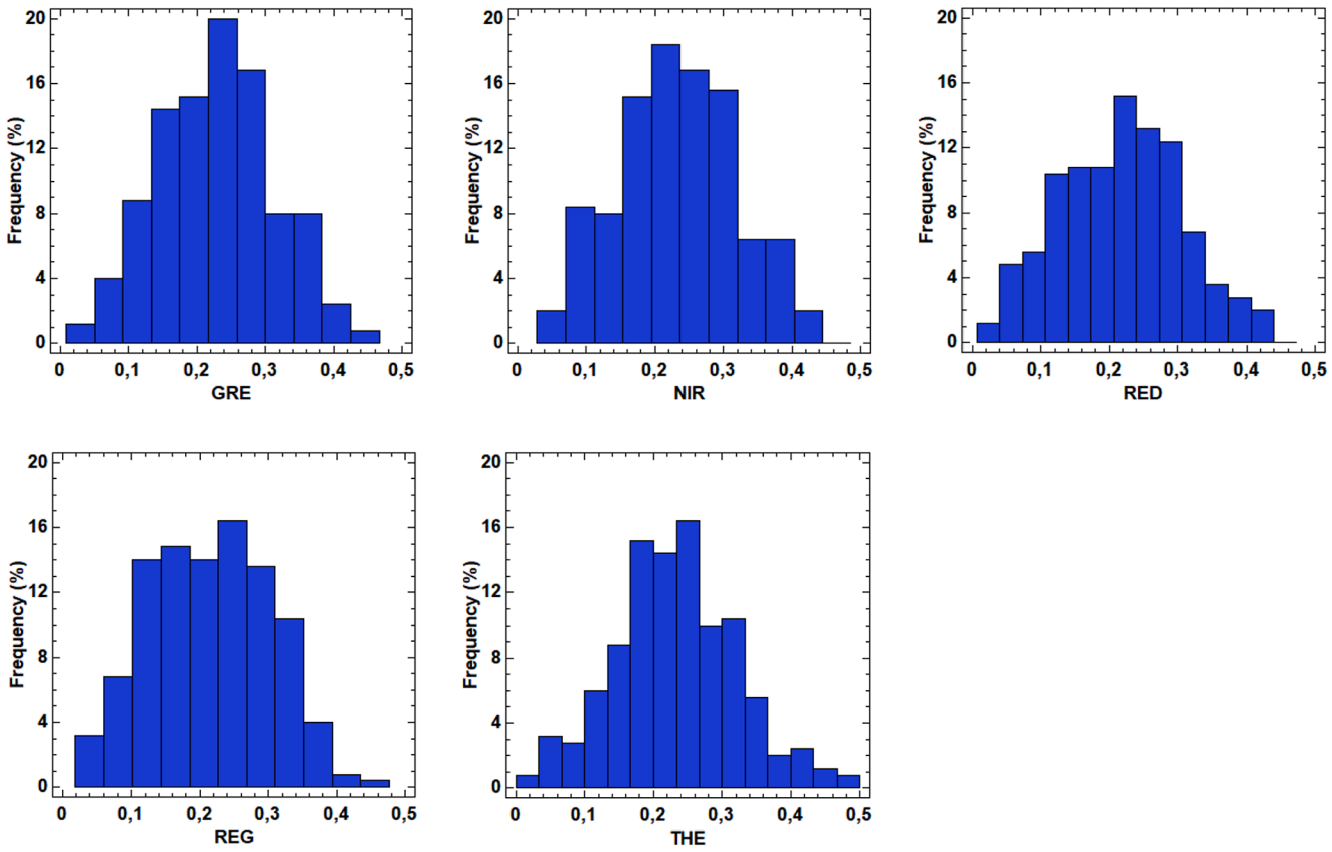

Fig. 14. *AI* frequency histograms for each band. All histograms show a typical shape of a normal distribution, which is confirmed by standard skewness and standard kurtosis values within the range −2 to + 2.

Sulik and Long [32] and Torres-Sánchez et al. [33] used the post-processing software PixelWrench 2 on images taken with Tetracam cameras, but no quantitative analysis are shown, only visual comparisons are provided. Kelcey and Lucier [34] proposed the use of an affine transformation for band co-registration of a Tetracam MiniMCA-6 camera, but they did not provide a quantitative accuracy analysis. Using the same camera, Laliberte et al. [35] reported sub-pixel band co-registration accuracy, obtained when a method based on a local weighted mean transform to detect the edges and matching conjugates lines was used for this task. Jhan et al. [25] proposed a modified projective transformation mathematical model for Tetracam MiniMCA-12 band co-registration. They compared the errors yielded by the software PixelWrench 2 (from 1.23 to 3.81 pixels) with the new proposed method (from 0.17 to 0.48 pixels). These same authors [27] developed a single image registration method (called RABBIT) that can co-register original multi-spectral images preserving the central perspective projection. For close-range applications this method yielded an average accuracy of 0.38 pixels and therefore, the band co-registered multi-spectral images can be utilized to generate a 3D model of any index derived from the bands. The methodology exposed in the present work does not maintain the central perspective in the resulting images because it is designed to be applied to objects with a small height located on a practically flat surface. Under these conditions, our methodology yielded an accuracy which also allows to derive indices from the utilized bands for agricultural purposes.

Yang et al. [36] implemented first- and second-order geometric transformation functions for band co-registration between two cameras. The coefficients of these transformations were solved measuring 4 to 10 conjugated control points manually identified in both images. These authors reported an accuracy of 5 to 8 pixels for the first-order transformation and 0.4 to 0.7 pixels for the second-order transformation. Li et al. [37][used the Scale Invariant Feature Transform (SIFT) algorithm for the band co-registration of a system consisting of four cameras and reported accuracies of 2.5 pixels.

4. Conclusions

This work proposes a methodology to band co-registration based on rectified images taken from several sensors and to study its accuracy in a quantitative way.

First, the results yielded in this work show an alternative to bypass the limitations of the orthorectification process related to the movement of the photographed objects. This limitation is present when it is necessary to have an orthoimage of a crop: even a light wind results in plant movement, and therefore, in each of the pictures, the plants will be in a different position.

Second, the rectification methodology exposed, based on lens distortion and perspective distortion corrections, a high and similar accuracy level for all studied sensors. The index used to assess the accuracy, *AI*, which represents, for a given band, the proportion of area of a digitalised edge plant out of the common area of the edge of each band, ranged from 0.22 to 0.24, with no statistically significant differences between bands.

Although in this work, the photographs were taken from a platform carried by an operator, this methodology is applicable to photographs taken by sensors fitted on UAVs or on terrestrial vehicles.

Further works could be oriented to study:

- the accuracy of this methodology to obtain mosaics from rectified images, thereby enlarging the study area,
- the variation of the precision of the lens distortion correction as the size of the used grid in decreases, as well as the use of other

interpolation methods differents to inverse distance to a square power to estimate ε_X and ε_Y.

Declaration of Competing Interest

The authors declare that they have no known competing financial interests or personal relationships that could have appeared to influence the work reported in this paper.

References

[1] M. Mayerová, J. Soukup, E ff ect of chemical weed control on crop yields in di ff erent crop rotations in a long-term fi eld trial, 114 (2018) 215–222. https://doi.org/10.1016/j.cropro.2018.08.001.

[2] A. Piron, V. Leemans, O. Kleynen, F. Lebeau, M. Destain, Selection of the most efficient wavelength bands for discriminating weeds from crop, 2 (2007) 141–148. https://doi.org/10.1016/j.compag.2007.12.007.

[3] L.M. Dale, A. Thewis, C. Boudry, I. Rotar, S.P. Florin, O. Abbas, P. Dardenne, V. Baeten, P. James, J.A. Fernández, Talanta Discrimination of grassland species and their classi fi cation in botanical families by laboratory scale NIR hyperspectral imaging : Preliminary results, 116 (2013) 149–154. https://doi.org/10.1016/j.talanta.2013.05.006.

[4] R.S. Fletcher, K.N. Reddy, Random forest and leaf multispectral reflectance data to differentiate three soybean varieties from two pigweeds, Comput. Electron. Agric. 128 (2016) 199–206, https://doi.org/10.1016/j.compag.2016.09.004.

[5] S. Akbarzadeh, A. Paap, S. Ahderom, B. Apopei, K. Alameh, Plant discrimination by Support Vector Machine classi fi er based on spectral re fl ectance, 148 (2018) 250–258. https://doi.org/10.1016/j.compag.2018.03.026.

[6] N. Kobayashi, H. Tani, X. Wang, R. Sonobe, Crop classification using spectral indices derived from Sentinel-2A imagery, J. Inf. Telecommun. (2019) 1–24, https://doi.org/10.1080/24751839.2019.1694765.

[7] Diario Oficial de la Unión Europea, Reglamento (CE) no 1107/2009 del Parlamento Europeo y del Consejo, de 21 de octubre de 2009, relativo a la comercialización de productos fitosanitarios y por el que se derogan las Directivas 79/117/CEE y 91/414/CEE del Consejo, 2009. http://data.europa.eu/eli/reg/2009/1107/oj.

[8] A. Tasistro, Métodos para evaluar efectividad en el control de malezas, Rev. Mex. La Cienc. La Maleza. Especial (2000) 25–35.

[9] F.A. Vega, F.C. Ramírez, M.P. Saiz, F.O. Rosúa, Multi-temporal imaging using an unmanned aerial vehicle for monitoring a sunflower crop, Biosyst. Eng. 132 (2015) 19–27, https://doi.org/10.1016/j.biosystemseng.2015.01.008.

[10] S.O. Ihuoma, C.A. Madramootoo, Crop re fl ectance indices for mapping water stress in greenhouse grown bell pepper, Agric. Water Manag. 219 (2019) 49–58, https://doi.org/10.1016/j.agwat.2019.04.001.

[11] S. Moharana, S. Dutta, Estimation of water stress variability for a rice agriculture system from space-borne hyperion imagery, Agric. Water Manag. 213 (2019) 260–269, https://doi.org/10.1016/j.agwat.2018.10.001.

[12] K. Klem, J. Záhora, P. Trunda, T. Ivan, P. Hoda, B. Rapantová, J. Hanu, J. Vav, P. Holub, Interactive e ff ects of water de fi cit and nitrogen nutrition on winter wheat, Remote sens. Meth. Detect. 210 (2018) 171–184, https://doi.org/10.1016/j.agwat.2018.08.004.

[13] M. Hou, F. Tian, T. Zhang, M. Huang, Evaluation of canopy temperature depression, transpiration, and canopy greenness in relation to yield of soybean at reproductive stage based on remote sensing imagery, Agric. Water Manag. 222 (2019) 182–192, https://doi.org/10.1016/j.agwat.2019.06.005.

[14] W. Su, M. Zhang, D. Bian, Z. Liu, J. Huang, W. Wang, J. Wu, H. Guo, Phenotyping of corn plants using unmanned aerial vehicle (UAV) images, Remote Sens. 11 (2019) 1–19, https://doi.org/10.3390/rs11172021.

[15] R. Ehsani, S. Sankaran, J.M. Maja, J. Camargo Neto, Affordable multi-rotor remote sensing platform for applications in precision horticulture, 11th Int, Conf. Precis. Agric. (2012).

[16] G. Yang, J. Liu, C. Zhao, Z. Li, Y. Huang, Unmanned Aerial Vehicle Remote Sensing for Field-Based Crop Phenotyping : Current Status and Perspectives, 8 (2017). https://doi.org/10.3389/fpls.2017.01111.

[17] H. Aasen, A. Burkart, A. Bolten, G. Bareth, ISPRS Journal of Photogrammetry and Remote Sensing Generating 3D hyperspectral information with lightweight UAV snapshot cameras for vegetation monitoring : From camera calibration to quality assurance, ISPRS J. Photogramm. Remote Sens. 108 (2015) 245–259, https://doi.org/10.1016/j.isprsjprs.2015.08.002.

[18] P.P.J. Roosjen, B. Brede, J.M. Suomalainen, H.M. Bartholomeus, L. Kooistra, J.G.P. W. Clevers, Int J Appl Earth Obs Geoinformation Improved estimation of leaf area index and leaf chlorophyll content of a potato crop using multi-angle spectral data – potential of unmanned aerial vehicle imagery, Int. J. Appl. Earth Obs. Geoinf. 66 (2018) 14–26, https://doi.org/10.1016/j.jag.2017.10.012.

[19] Y. Ampatzidis, V. Partel, UAV-based high throughput phenotyping in citrus utilizing multispectral imaging and artificial intelligence, Remote Sens. 11 (2019), https://doi.org/10.3390/rs11040410.

[20] R. Darvishzadeh, C. Atzberger, A. Skidmore, M. Schlerf, ISPRS Journal of Photogrammetry and Remote Sensing Mapping grassland leaf area index with airborne hyperspectral imagery : A comparison study of statistical approaches and inversion of radiative transfer models, ISPRS J. Photogramm. Remote Sens. 66 (2011) 894–906, https://doi.org/10.1016/j.isprsjprs.2011.09.013.

[21] T.R.W. Hunt, E.R. Jr, D.A. Horneck, P.B. Hamm, D.J. Gadler, A.E. Bruce, Detection of nitrogen deficiecy in potatoes using small unmanned air craft systems. in, twelth Int., Conf. Precis. Agric, Sacramento, California, USA, 2014.

[22] P. McKenna, P.D. Erskine, A.M. Lechner, S. Phinn, Measuring fire severity using UAV imagery in semi-arid central Queensland, Australia, Int. J. Remote Sens. 38 (2017) 4244–4264, https://doi.org/10.1080/01431161.2017.1317942.

[23] K. Novak, Rectification of Digital Imagery, Photogramm. Eng. Remote Sens. 5 (1993) 339–344.

[24] M. Shahbazi, C. Cortes, SEAMLESS CO-REGISTRATION OF IMAGES FROM MULTI-SENSOR MULTISPECTRAL CAMERAS, XLII (2019) 2–3.

[25] J.P. Jhan, J.Y. Rau, C.Y. Huang, Band-to-band registration and ortho-rectification of multilens/multispectral imagery: A case study of MiniMCA-12 acquired by a fixed-wing UAS, ISPRS J. Photogramm. Remote Sens. 114 (2016) 66–77, https://doi.org/10.1016/j.isprsjprs.2016.01.008.

[26] J.P. Jhan, J.Y. Rau, N. Haala, M. Cramer, Investigation of parallax issues for multi-lens multispectral camera band co-registration, Int. Arch. Photogramm. Remote Sens. Spat. Inf. Sci. - ISPRS Arch. 42 (2017) 157–163, https://doi.org/10.5194/isprs-archives-XLII-2-W6-157-2017.

[27] J.P. Jhan, J.Y. Rau, N. Haala, Robust and adaptive band-to-band image transform of UAS miniature multi-lens multispectral camera, ISPRS J. Photogramm. Remote Sens. 137 (2018) 47–60, https://doi.org/10.1016/j.isprsjprs.2017.12.009.

[28] B. Zitová, J. Flusser, Image registration methods: A survey, Image Vis. Comput. 21 (2003) 977–1000, https://doi.org/10.1016/S0262-8856(03)00137-9.

[29] F.R.G.B. Imagery, A. Habib, Y. Han, W. Xiong, F. He, Z. Zhang, Automated Ortho-Rectification of UAV-Based Hyperspectral Data over an Agricultural Field Using, (2016) 1–22. https://doi.org/10.3390/rs8100796.

[30] M. Louargant, G. Jones, R. Faroux, J. Paoli, T. Maillot, G. Christelle, S. Villette, Unsupervised Classification Algorithm for Early Weed Detection in Row-Crops by Combining Spatial and Spectral, Information (2018) 1–18, https://doi.org/10.3390/rs10050761.

[31] S. Jakob, R. Zimmermann, R. Gloaguen, The Need for Accurate Geometric and Radiometric Corrections of Drone-Borne Hyperspectral Data for Mineral Exploration: MEPHySTo-A Toolbox for Pre-Processing Drone-Borne Hyperspectral Data, Remote Sens. 9 (2017), https://doi.org/10.3390/rs9010088.

[32] J.J. Sulik, D.S. Long, Spectral considerations for modeling yield of canola, Remote Sens. Environ. 184 (2016) 161–174, https://doi.org/10.1016/j.rse.2016.06.016.

[33] J. Torres-Sánchez, F. López-Granados, A.I. De Castro, J.M. Peña-Barragán, Configuration and Specifications of an Unmanned Aerial Vehicle (UAV) for Early Site Specific Weed Management, PLoS ONE 8 (2013), https://doi.org/10.1371/journal.pone.0058210.

[34] J. Kelcey, A. Lucieer, Sensor correction of a 6-band multispectral imaging sensor for UAV remote sensing, Remote Sens. 4 (2012) 1462–1493, https://doi.org/10.3390/rs4051462.

[35] A.S. Laliberte, M.A. Goforth, C.M. Steele, A. Rango, Multispectral remote sensing from unmanned aircraft: Image processing workflows and applications for rangeland environments, Remote Sens. 3 (2011) 2529–2551, https://doi.org/10.3390/rs3112529.

[36] C. Yang, B. Fritz, W. Hoffmann, Y. Lan, D. Martin, C. Suh, J. Westbrook, J. Goolsby, An Airborne Multispectral Imaging System Based on Two Consumer-Grade Cameras for Agricultural Remote Sensing, Remote Sens. 6 (2014) 5257–5278, https://doi.org/10.3390/rs6065257.

[37] H. Li, A. Zhang, S. Hu, A multispectral image creating method for a new airborne four-camera system with different bandpass filters, Sensors (Switzerland). 15 (2015) 17453–17469, https://doi.org/10.3390/s150717453.